

Interpolated Mechanics—Molecular Mechanics Study of Internal Rotation Dynamics of the Chromophore Unit in Blue Fluorescent Protein and Its Variants

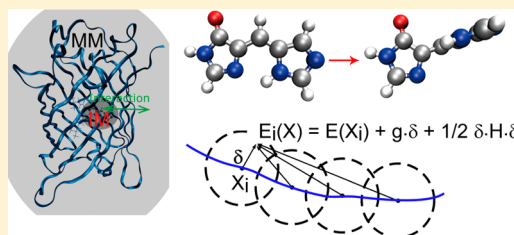
Jae Woo Park and Young Min Rhee*

Department of Chemistry, Pohang University of Science and Technology (POSTECH), Pohang 790-784, Korea

S Supporting Information

ABSTRACT: The excited state dynamics of the blue fluorescent protein (BFP) and its variants, azurite, EBFP1.2, and EBFP2.0, are studied using molecular dynamics (MD) simulations on potential energy surfaces (PESs) generated with the interpolated mechanics—molecular mechanics (IM/MM) scheme. This IM/MM strategy adopts the interpolated PES for an important area of the complex and the conventional force field for the remaining part. We focus on the internal rotation dynamics of the chromophore unit, which is directly related to its fluorescence property, and analyze the time evolutions of the nonrotated chromophore fractions based

on trajectories over 10 μ s of aggregate simulation time. The characteristics obtained from the calculated time progresses of the nonrotated chromophore fractions in BFP and other variants agree well with experimentally observed properties. The results show that the MD simulation with an IM/MM potential is an attractive approach for studying excited state dynamics of fluorescent proteins in consideration of its efficiency and reliability. We also attempt to investigate the detailed roles that the mutated residues play in delaying the excited state chromophore twisting and thus improving the fluorescence property, and discuss the contributions by the Coulombic and the steric interactions between the chromophore and the mutated residues.



1. INTRODUCTION

Molecular dynamics (MD) simulation is a frequently adopted technique for observing various biophysical phenomena.^{1–3} Especially, it is a commonly used method in investigating dynamic features of macromolecules in biological systems such as proteins, nucleic acids, or lipids. In these macromolecular systems,⁴ nonbonded interactions mainly govern the dynamics and are described in detail. Bonded interactions are conventionally described with simple potential functions, such as the harmonic oscillator model or the Morse potential.^{5–7} However, for dynamics involving large distortions from stable conformations of any molecules, this type of simple models may not be sufficient. Particularly, in the electronically excited state, the most stable geometry may be far away from the equilibrium ground state geometry. Therefore, anharmonicity of the potential energy surface becomes important. In the case of photoproteins, electronic excitations need to be considered, and without an improved description of the potential energy surfaces, one cannot study their photodynamics in an appropriate manner.

One of the best examples of systems that involve the excited state dynamics will be fluorescent proteins (FPs). Indeed, FPs have served as important molecular imaging and analysis tools in biology over the last few decades.^{8–27} However, their photodynamics is not easily accessed and the related studies from the viewpoint of theoretical/computational approaches have been reported somewhat scarcely even though many important insights have been attained through theoretical studies.^{25–33} This is mainly because the computational cost of

obtaining an excited state potential energy surface (PES) tends to be too high in the practical sense when it is obtained with reliable quantum chemical methods. Moreover, in the case of studying proteins, MD simulations over a few nanoseconds are usually needed,²⁴ which may render the computational burden even severer. Of course, analytically modeling the surface may avoid the problem associated with the length of dynamics simulations. For example, Jonasson et al. recently conducted a set of 24 simulations of the green fluorescent protein (GFP) over 15 ns durations using an empirical potential energy function of two torsional angles of the chromophore.²⁴ However, simple analytical functions may not be sufficiently adequate especially because there are many degrees of freedom in the fluorophore unit. When the molecule of interest becomes larger, this issue will likely become more important.

More accurate methods such as mixed quantum mechanics/molecular mechanics (QM/MM) in combination with *ab initio* molecular dynamics (AIMD) can be an alternative option. For short-time dynamics (up to 10 ps) of FPs, there indeed are examples of treating chromophores with quantum chemical methodologies.^{26,30} However, especially for the excited state dynamics, the associated computational cost will still be prohibitively high in the case of long-time dynamics. In this regard, one can resort to an alternative approach based on a model using an interpolated potential energy surface. In this

Received: June 25, 2012

Revised: August 9, 2012

Published: August 14, 2012

interpolation scheme, which was first introduced by Collins and co-workers,^{34–36} the energy at a given geometry is calculated as a weighted interpolation of local Taylor expansions from different origins (“data points”). Initially, it was mainly used for studying gas phase reactions.^{34–44} Its extension to studying large molecular complexes in condensed phases was further explored by Truhlar and co-workers⁴⁵ within the context of combining the electrostatically embedded multiconfiguration molecular mechanics (EE–MCMM) method^{46,47} and conventional molecular mechanics (MM). The MCMM approach employs interpolation for constructing off-diagonal elements of the Hamiltonian so that its lowest eigen-energy can closely mimic the reference QM/MM values globally.⁴⁸ Additional schemes for applying the interpolation technique in building the diagonal energy term for studying condensed phase dynamics have also been reported very recently.⁴⁹

In this article, we demonstrate this interpolated potential energy surface scheme can also be applied to treating a subgroup of atoms (which needs detailed and more accurate descriptions of the potential energy, such as chromophores or catalytic triads) in a biological macromolecular complex. We will name this method “interpolated mechanics/molecular mechanics (IM/MM)” in an analogy to QM/MM, as the remaining part of the complex is treated with a molecular mechanics approach with a conventional force field. Particularly, we study the excited state dynamics of the blue fluorescent protein (BFP, Figure 1) and its variants using classical MD with IM/MM potential surfaces. BFP was generated by substituting the tyrosine-66 residue of GFP into histidine,^{9–13,27} so that its modified conjugated structure can present blue fluorescence. In fact, many variants have been developed to enhance its quantum yield and photostability.^{11–14} As detailed molecular pictures with such variants are still lacking, the photodynamics of BFP will be an interesting target for study. As a first presentation of the IM/MM scheme, in the present work, we will intentionally avoid investigating full excited state features such as surface crossing and the related nonadiabatic aspects. Instead, we will focus on the internal twisting of the chromophore part with classical MD simulations on a single surface, assuming that the internal rotation almost instantly leads to a nonadiabatic and nonradiative internal conversion down to the electronic ground state. (We note that applying the interpolation scheme for full nonadiabatic dynamics is also possible. See refs 50 and 51, for example.) With such dynamics, various interesting features of BFP photodynamics are still observed. On the basis of such observations, we will explain why different photodynamic features appear for different variants of BFP. Ultimately, similar explanations may lead to a prospect for designing new FPs with enhanced functionalities. We will conclude the paper by discussing the strengths and weaknesses of the IM/MM scheme as a general research tool for many other photoproteins, and potential future developments for overcoming the weaknesses.

2. METHODS

Interpolated Potential Energy Surface. For completeness, we will briefly overview the interpolation technique adopted in this work. More details of the methodology can be found in refs 34–36 and 49. The overall potential energy V used for the molecular simulations is written as

$$V = V_I + V_{\text{disp}} + V_{\text{coul}} \quad (1)$$

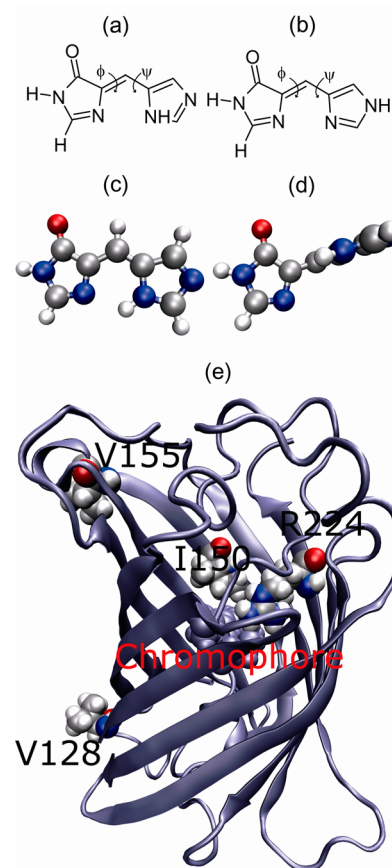


Figure 1. The graphical representations of the systems studied in this article. Structures of (a) the blue fluorescent protein chromophore with histidine-D type protonation (HID/BFPC) and (b) the blue fluorescent protein chromophore with histidine-E type protonation (HIE/BFPC). (c) Ground state optimized structure of HID/BFPC and (d) ϕ -rotated geometry of HID/BFPC. (e) A cartoon representation of the blue fluorescent protein and the positioning of the chromophore. The four mutated residues in EBFP2.0 are shown in space-fill model.

Here, V_I is the intramolecular potential energy of the molecule(s) in the interpolation region. V_{disp} is the Lennard-Jones dispersion energy, and V_{coul} is the electrostatic energy between the interpolation region and the remainder of the system. V_I is written as

$$V_I(\mathbf{Z}) = \sum_a^N w_a(\mathbf{X}) V_a(\mathbf{Z}) \quad (2)$$

where $w_a(\mathbf{X})$ is the interpolation weighting function. The potential energy calculated as a local expansion, V_a , is given as

$$V_a(\mathbf{Z}) = V(\mathbf{Z}_a) + \Delta_a^T \cdot \mathbf{g}_a + \frac{1}{2} \Delta_a^T \cdot \mathbf{H}_a \cdot \Delta_a \quad (3)$$

In this formula, $V(\mathbf{Z}_a)$ is the potential energy at the a th data point and \mathbf{g}_a and \mathbf{H}_a are first and second derivatives of the potential. Δ_a is the geometry difference between the data point \mathbf{Z}_a and an arbitrary geometrical point \mathbf{Z} .

We need to obtain the first and second derivatives at all data points to obtain V_I and its gradient. However, especially for the second derivatives, the associated computational cost with accurate excited-state quantum chemistry methods such as

complete active space second-order perturbation theory (CASPT2)⁵² is usually too high in the practical sense. To circumvent this problem, we have adopted an approach developed by Nguyen et al. that utilizes the dual-level scheme for the PES construction.³⁷ In this dual-level interpolation formalism, the potential energy is written as

$$V_{I,C}(\mathbf{Z}) = V_I(\mathbf{Z}) + V_C(\mathbf{Z}) \quad (4)$$

where V_I is the interpolated potential energy calculated using the data set from a low-level quantum chemistry method given by eqs 2 and 3 and V_C is the correction term defined as

$$V_C(\mathbf{Z}) = \sum_a^N w_a(\mathbf{X})(V_{HL}^a - V_{LL}^a)(\mathbf{Z}) \quad (5)$$

Here, V_{HL}^a is the potential energy of a data point a calculated with a high-level quantum chemistry method and V_{LL}^a is the potential at the same point obtained by a low-level quantum chemistry method. Now, the collection of $V_{HL}^a - V_{LL}^a$ and their gradients compose another data set, which is used for the calculation of V_C . During MD simulations, V_I and V_C are separately computed and then combined for constructing the potential energy surface.

Because the interpolation region (in our case, the chromophore) is covalently connected to the protein backbone, we need a “link atom” between the region and the protein backbone. This situation is similar to the case in QM/MM.^{53,54} For energy conservation, the force that acts on the link atom should also be exerted on the frontier atom in the protein backbone. Following the common convention, the link atoms are added to the IM area as hydrogen for the QM calculations associated with the data set construction.

Parametrization and Construction of the Data Set for Interpolation. We have used the BFP chromophore structure with δ -nitrogen protonated histidine (HID/BFPC) (Figure 1a) rather than with ϵ -nitrogen protonated histidine (HIE/BFPC) (Figure 1b), as the excitation energy calculated by the SAC-CI method for HID/BFPC was reported to be closer to the experimental excitation energy of BFP.²⁷ For the state-averaged complete active space self-consistent field (SA-CASSCF)⁵⁵ calculations, we need to define an appropriate active space for static electron correlations. For this purpose, we tested a series of active spaces, from (2,2) to (12,12), by scanning the electronic energy of BFPC with two torsional angles ψ and ϕ . Here, of course, (n,m) denotes the correlation scheme with n electrons in m active orbitals. These torsional angles are equivalent to the phenol bridge and the imidazolinone bridge dihedral angles, respectively, in the GFP model chromophore of *p*-hydroxybenzylideneimidazoline (*p*-HBI).^{24–26} They are also accepted to play a key role in the photodynamics of the fluorescent proteins.^{20–26} On the basis of these scanned energies, we chose the (4,4) space as the appropriate one with a balance between reliability and efficiency. The detailed comparisons will be provided in the next section.

Now, the ground and excited state geometries of BFPC are optimized at the level of SA2-CAS(4,4)⁵⁵ with the ANO-RCC-VDZP basis set.^{56,57} Using these optimized geometries, the second-order corrected (SA2-CAS(4,4)-PT2) relaxed one-particle density matrices were calculated to obtain restrained electrostatic potential (RESP) atomic charges⁵⁸ for both ground and excited states. To calculate Lennard-Jones parameters, the argon scanning approach,⁵⁹ as has been adopted with other chromophore molecules as coumarin-

153⁴⁹ and oxyluciferin,⁶⁰ was applied. An argon atom was placed successively on 687 and 685 grid points in ground and excited states. The grid points form eight shells within a distance range of 2.5–13.0 Å from the atoms of BFPC. The electronic energies were calculated for these geometries at the SA2-CAS(4,4)-PT2/ANO-RCC-VDZP level, and the Lennard-Jones parameters were fitted to these electronic energies with the same process described in ref 59.

The data set for the interpolation was constructed as follows. First, we obtained 19 initial geometries by varying the torsional angle ϕ from the S_1 optimized geometry within the 0–90° range. The S_0 optimized geometry was added to the set, expanding it to a total of 20 initial points. Then, four sets of new geometries are subsequently added to improve the S_1 PES. To construct these sets, we conducted MD simulations for BFPC in various conditions listed in Table 1. Each time when

Table 1. List of Simulation Conditions during the Interpolation Data Set Construction and the Number of Data Points Obtained

round	number ^a	distance ^b (Å)	in protein ^c	temperature ^d (K)
1	50	0.5	no	0
2	50	0.5	no	300
3	100	0.5	yes	300
4	54	1.0	no	300

^aNumber of data points obtained from each data set construction round. ^bDistance cutoff from pre-existing data points for deciding to add a new data point. ^cWhether the simulations were performed with the surrounding protein. “No” designates that the simulations were conducted in the gas phase with the bare chromophore. ^dThe temperature adopted for generating random initial velocity.

the trajectory reaches a conformation that was farther from all existing data points than a preset cutoff distance, the conformation was added to the data set. The total number of data points added in each condition is also shown in Table 1, together with the cutoff criterion in each case. Of course, after obtaining a conformation, we calculated its energy, gradient, and Hessian as interpolation data. With the data points thus collected, finally, we conducted ground state gas phase MD simulations of BFPC with initial velocity corresponding to 300 K in order to improve the S_0 PES, and added 10 geometries which were farther than a cutoff distance of 0.5 Å from other data points. In the end, we have obtained 284 data points for the construction of the S_1 PES. Energy, gradient, and Hessian for any data point were calculated at the SA2-CAS(4,4)/6-31+G* level.⁶¹ All quantum chemical calculations were conducted with MOLPRO.⁶²

Ideally, the above procedures can be processed in an automatic manner. However, for practical reasons, we included one manual adjustment. CASSCF solutions have a tendency of showing a local minima issue because of its nonlinear nature of the orbital or electronic energy optimizations.^{63,64} These multiple solutions differ not only in energy but of course in its gradient and Hessian. Especially when the Hessian is obtained via numerical differentiations, this multiple solution problem leads to an unphysical asymmetric Hessian. If a Hessian matrix of energy is asymmetric, PES will ill-behave and the corresponding dynamics will be erratic. Thus, we always inspected the nature of the Hessian matrix, and whenever any asymmetry was found, the database update was interrupted until proper CASSCF solution was found. The details on

Table 2. List of Adopted Model BFP Variants, Their Mutated Residues, Fluorescence Quantum Yields, and the Lifetimes^a

variant	mutation ^b	quantum yield	fluorescence lifetime (ns)
BFP		0.34 ¹¹ 0.24 ¹⁸ 0.20 ⁷⁴	2.82 ¹¹ 2.4 ⁷⁴
azurite	BFP+R80Q,Y145F,V150I,V224R	0.55 ¹¹ 0.59 ¹²	3.65 ¹¹ 3.4 ± 0.2 ⁷⁷
EBFP1.2	BFP+S30R,Y39N,S72A,N105T,Y145F,I171V,N198S,A206V	0.45 ¹² 0.38 ⁷⁸	2.16 ⁷⁸
EBFP2.0	EBFP1.2+I128V,V150I,D155V,V224R	0.36 ⁷⁹ 0.56 ¹² 0.71 ⁷⁸ 0.64 ⁷⁹	3.65 ⁷⁸ 3.0 ± 0.2 ⁷⁷

^aExperimental numbers are taken from references explicitly cited in the table. ^bMutations are denoted as X_nY when the *n*th residue X is mutated to Y.

reaching a well-behaved CASSCF solution are described in the Supporting Information.

To improve the *S*₁ potential surface at the SA2-CAS(4,4) level, we additionally performed SA2-CAS(4,4)-PT2 calculations with the 6-31+G* basis set.⁶¹ The potential energies and the gradients were added to the database for the dual level interpolation. On one of the data points, the PT2 calculation did not converge and the point was omitted from dual level improvement set. The energies and the gradients calculated with SA2-CAS(4,4)/6-31+G* are subtracted from the corresponding SA2-CAS(4,4)-PT2 values, and the differences are collected as a secondary data set for the dual-level interpolation described in section 2.

Simulation Details. Computational code for constructing dual-level interpolated PES was implemented in the form of an external library. The GROMACS 4.0 package⁶⁵ was employed for simulations with the AMBER99SB^{5,66} force field, which is known to give better secondary structures.⁵ Water molecules were represented with the rigid three-point model TIP3P. Lennard-Jones and Coulomb interactions were considered with 12.0 Å cutoffs with 10.0 Å tapers. The integration step size was 2.0 fs for all simulations, and all bonds containing hydrogen atoms were constrained with the LINCS algorithm.⁶⁷ Of course, constraining bonds stabilizes the dynamics not only with the classical harmonic model but also with the interpolated PES.⁴⁹

Initially, the structure of BFP was obtained from the relevant crystallographic structure (PDB ID: 2EMD).⁶⁸ For its variants, modified geometries were generated by replacing the side chain atoms using the PDB2PQR program.⁶⁹ The variants adopted in this work are listed in Table 2 together with a detailed list of mutated residues. The simulation box was obtained by solvating BFP or its variants in a cubic box of 60 Å side lengths. In addition, an isolated BFP model chromophore was solvated in water with a periodic boundary box of 50 Å side lengths. For each of the solvated systems, the energy was minimized using the steepest descent method.⁷⁰ With these geometries, equilibration runs of 50 ps duration were performed at the isothermal–isobaric (*NPT*) condition. The pressure and temperature were kept by Berendsen's weak coupling thermostat and barostat algorithms,⁷¹ to reach the target temperature of 300 K and the target pressure of 1 bar. After this, the geometries were equilibrated for an additional 50.0 ps duration after switching to the Nosé–Hoover thermostat⁷² and the Parrinello–Rahman barostat⁷³ algorithms. After these pre-equilibrations, 500 equilibrated ground-state geometries were

generated at 2.0 ps intervals from a 1.0 ns simulation. Then, starting from these 500 conformations for BFP and its variants, a set of as many nonequilibrium simulations were run for 2.0 ns for each trajectory on the excited state potential energy surface.

In addition to the above, we focused on the characteristic differences of EBFP2.0 over EBFP1.2. Although EBFP2.0 shows far enhanced fluorescence (Table 2), these two proteins differ only in four amino acid residues. Thus, by investigating these four mutations (I128V, V150I, D155V, and V224R) individually, it will be possible to unravel the role of the protein environment on improving fluorescence at a relatively low computational cost. Also, to inspect the functions of electrostatic and dispersive interactions separately, we generated an electrostatic mutant of EBFP1.2 and EBFP2.0 by eliminating atomic partial charges of the mutated sites. For all of these additional protein systems, the same simulation protocols as described in the above were applied to generate the nonequilibrium trajectories. In total, the aggregate simulation times for all nonequilibrium trajectories were well over 10.0 μs.

Our notations for residue indices and mutant distinctions as adopted in Figure 1 and Table 2 might be confusing, as they are somewhat similar in appearances. To avoid potential confusions, let us clarify the notations before discussing our results. Throughout this paper, a mutant protein is designated as X_nY when the amino acid X at the *n*th residue is mutated to an amino acid Y, with standard one-letter representations of amino acids. Multiple mutations can be denoted with this scheme without any ambiguity. For instance, BFP+R80Q in Table 2 represents mutation from arginine to glutamine on the 80th residue of BFP. The four mutant proteins of EBFP1.2, namely, I128V, V150I, D155V, and V224R, will be denoted without showing EBFP1.2 explicitly for simplicity. On the other hand, X_n designates the *n*th amino acid X in a given protein. For example, I150 in Figure 1 represents the isoleucine-150 in EBFP2.0. These notations will be consistently used in the following discussions on our simulation results.

3. RESULTS AND DISCUSSION

Potential Energy Surface of BFP Chromophore. Figure 2 shows the potential energy scans over the two dihedral angles ϕ and ψ , from SA-CASSCF calculations with various active orbital spaces. In the case of the ϕ -angle, active space schemes of (2,2), (4,4), (10,10), and (12,12) were used, while (2,2), (4,4), and (10,10) were adopted for ψ . For the case of angle ϕ (Figure 2a), overall potential profiles are quite similar to each other except for some ruggedness observed with a few points

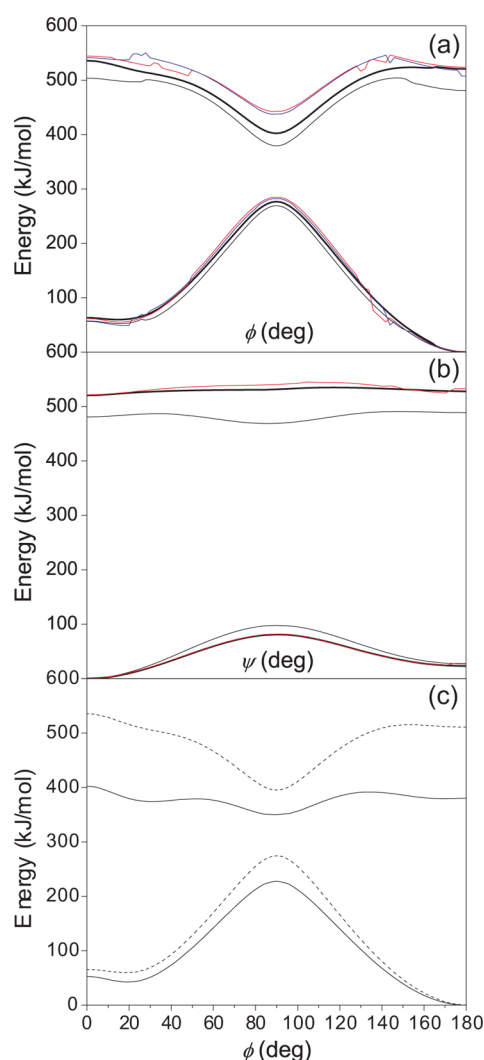


Figure 2. Potential energy scans over dihedral angles: (a) SA2-CAS potential energy over ϕ torsion. The adopted active space schemes are (2,2) (solid black), (4,4) (dashed black), (10,10) (red), and (12,12) (blue). (b) SA2-CAS potential over ψ torsion with (2,2) (solid black), (4,4) (dashed black), and (10,10) (red) active space schemes. (c) Comparison of SA2-CAS(4,4)-PT2 (solid lines) and SA2-CAS(4,4) (dashed lines) potential energies.

that lie out of the lines. These outlying points reflect the occasional incorrect convergence of the orbital optimizations, which we intentionally left uncorrected as a direct illustration of the local minimum issue. Compared to the case of the ϕ angle, the potential along ψ exhibits a strong dependence on the nature of the active space used in SA-CASSCF calculations (Figure 2b). The most prominent feature is the fact that there is an artifactual potential energy barrier (~ 3 kJ/mol) around $\phi = -30^\circ$ with the small active space scheme, (2,2). With larger active spaces, this barrier simply disappears. In addition, with the (2,2) active space scheme, there appears a minimum on the S_1 potential energy surface around $\psi = -90^\circ$. This minimum also disappears with larger active spaces, and the potential energy is nearly flat with respect to the twisting around ψ . From the above behaviors of the PES, we have decided that the active space of (4,4) is the minimally acceptable level with qualitatively appropriate behaviors of the surface. The active orbitals included in SA2-CAS(4,4) calculations are π -style orbitals that span both imidazole and imidazolinone rings, and

this character is not highly sensitive to the internal twisting of the chromophore. However, the configuration interaction (CI) coefficients are somewhat sensitive to the twisting. This sensitivity will likely explain the lack of qualitative adequacy of the (2,2) scheme. For a more detailed discussion, see the Supporting Information along with Figure S1 and Table S1.

To correct for the dynamic electron correlation energies, the second order perturbation scheme of SA2-CAS(4,4)-PT2 was also applied. Figure 2c compares the energies from SA2-CAS(4,4)-PT2 and SA2-CAS(4,4) calculations. On the excited state surface, interestingly, we can observe ~ 10 kJ/mol barrier from the 20° conformer to the 90° conformer only with this correlation correction. Namely, when the chromophore is excited from the stable ground state geometry, it can only twist to the stable conformer on the excited state surface by passing through a small rotational barrier. This is also associated with the smaller twisting force in the excited state. Namely, in the excited state, the $\phi = 90^\circ$ geometry is 115 kJ/mol more stable than the $\phi = 0^\circ$ structure with SA2-CAS(4,4), while the same geometries differ in energy only by 30 kJ/mol with SA2-CAS(4,4)-PT2. Of course, the actual barrier and twisting force may become different if we conduct constrained optimizations at given torsional angles. Because our IM/MM scheme can automatically construct the accurate potential energy surface with increasing number of data points, obtaining the accurate barrier height value is not actually crucial. However, we can at least observe that the barrier height and the twisting force are largely affected by the inclusion of dynamic electron correlations. Thus, we can infer that taking account of the dynamic correlation effect with the SA2-CAS(4,4)-PT2 scheme is necessary in obtaining reliable dynamics of the chromophore. This is the reason for adopting the dual-level interpolation approach in this work. Because of the practical difficulty in calculating second derivatives of SA2-CAS(4,4)-PT2 energies, we have combined SA2-CAS(4,4) and SA2-CAS(4,4)-PT2 calculations during the interpolation. RESP charges and Lennard-Jones parameters are fitted to the quantum chemical calculation results as described in the previous section. Their numerical values are listed in Table S2 in the Supporting Information.

Excited State Dynamics of Chromophore in Protein Variants.

To investigate the fluorescence characteristics, we have mainly utilized the chromophore twisting behavior. This is based on an assumption that the nonradiative transition is extremely fast (compared to the fluorescence lifetime) once the chromophore reaches a rotated conformer space. This assumption is also supported by earlier quantum dynamics studies,^{24,26,28} which reported that population transfer is very rapid and efficient in condensed phase when the fluorophores reach twisted configurations. If we assume that this internal rotation is the only source of nonradiative decays, the fluorescence intensity at any given instance will be proportional to the fraction of chromophores that have not rotated up to that time point. Of course, in our simulation scheme at time zero, the chromophores follow the canonical distribution in the ground state, and the torsional angle will be mostly around $\phi = 180^\circ$. The chromophores are then impulsively promoted to the excited state and more and more will rotate toward $\phi = 90^\circ$ as time progresses. (See the potential shape shown in Figure 2.)

On the basis of the 500 independent trajectories for each BFP variant, we have calculated the fractions of the nonrotated chromophores with a 0.2 ps time resolution. An isolated chromophore molecule in water was also simulated for

comparison purposes. Along the trajectories, if the chromophore twisting reached $\phi = 100^\circ$, it was declared to have rotated. In fact, it is unlikely that a rotated chromophore will bounce back to a nonrotated conformation because of the rather large rotational barrier (~ 40 kJ/mol) on the SA2-CAS(4,4)-PT2 PES, as was shown in Figure 2c. Thus, the definition of the cutoff angle for declaring rotations is not actually important. Of course, in the experimental situation, rotated chromophores will not likely bounce back either, because, once it rotates, it will quickly fall down to the ground state through the fast nonradiative decay. We also confirmed that with our cutoff angle no trajectory returns from the rotated conformation back to the nonrotated side within our simulation time scale.

Figure 3 presents the fraction of nonrotated chromophores thus obtained. One can easily see that the nonrotated fraction

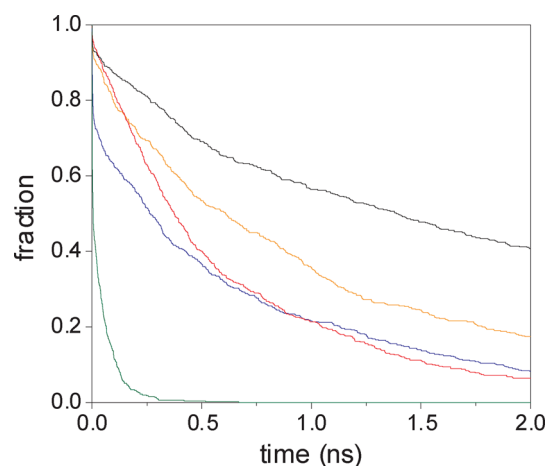


Figure 3. The fraction of nonrotated chromophores from 500 trajectories of BFP (blue), azurite (orange), EBFP1.2 (red), and EBFP2.0 (black). The bare chromophore solvated in water is also shown (green).

decays very fast in water, with a half-life of 4.2 ps. (The half-life is defined to be the time when the fraction reaches $f = 0.5$.) Interestingly, this result agrees well with the rotation time coefficient of 5.3 ps obtained with excited state GFP chromophore simulations based on a fitted analytical potential function.²⁴ Figure 3 also obviously shows that the rotation becomes slower when the chromophore is surrounded by the protein environment. Indeed, with experiment, the fluorescence lifetime and the quantum yield of the isolated chromophore were observed to be very different from the corresponding values of the chromophore within various fluorescent proteins,^{23,24} and our simulations are correctly reproducing this aspect.

Now, let us focus on the differences induced by protein variations. Their experimentally measured quantum yields and fluorescence lifetimes are listed in Table 2. Of course, all three variants have higher quantum yields than the original BFP, as they were designed for improvements. Among the three variants, the quantum yield is the highest with EBFP2.0 followed by azurite. The fluorescence lifetime is not that different with mutations, but we can see the lifetime is similarly longer with EBFP2.0 and azurite, while it is shorter with EBFP1.2. From our simulations, we can see that 20% of BFP chromophores have rotated after a short time of 3 ps. In all other variants, only 4–7% of the chromophores rotate in 3 ps.

In the longer time, the portion of rotated chromophores is largest with EBFP1.2 and BFP, followed by azurite and EBFP2.0. Thus, the trends in experimentally measured quantum yield and fluorescence lifetime agree reasonably well with our simulation results.

More quantitative comparison can be attained by converting the experimental data into rotational lifetimes. When both radiative and rotational nonradiative transitions are assumed to follow single exponential behaviors, the fluorescence lifetime can be decomposed into nonradiative and radiative lifetimes as

$$\frac{1}{\tau_{\text{fluo}}} = \frac{1}{\tau_{\text{rot}}} + \frac{1}{\tau_{\text{rad}}} \quad (6)$$

Also, from the quantum yield $\phi = \tau_{\text{fluo}}/\tau_{\text{rad}}$, the rotational lifetimes can be written as

$$\tau_{\text{rot}} = \frac{\tau_{\text{fluo}}}{1 - \phi} \quad (7)$$

The rotational lifetimes from average experimental data are shown in Table 3, together with our IM/MM-based rotational

Table 3. Rotational Lifetimes Calculated from Single Exponential Modeling Based on Experimental Data and IM/MM Simulations

	experiment ^a		IM/MM	
	τ_{rot}	rel. τ^b	τ_{rot}	rel. τ^b
BFP	3.53	1.00	0.61	1.00
azurite	8.20	2.32	0.88	1.44
EBFP1.2	3.58	1.01	0.57	0.93
EBFP2.0	9.15	2.59	1.09	1.79

^aBased on the average of data shown in Table 2. ^bRotational lifetimes relative to τ_{rot} of BFP.

lifetimes from simulations. In the simulation case, the rotational lifetimes were simply computed by fitting nonrotated chromophore fractions with single-exponential functions. Even though the simulated lifetimes are somewhat too short than the experimental values, one can see that the trend from simulations is in exact accord with experimentally observed features. It should be noted that we have adopted a minimally acceptable level of quantum chemical calculations, and the barrier height over the chromophore twisting was likely obtained not within the chemical accuracy. We believe that the chromophore internal rotations in our simulations happen somewhat more easily than in the experimental situation mainly due to this limitation in the adopted level of quantum chemical calculations. In fact, an error of only 1 kcal/mol in the barrier height can affect the reaction rate (in this case, the chromophore rotation) by about 5 times at room temperature. Another important cause of the discrepancy is the simplicity of our treatment on the nonadiabatic dynamics. For example, with Figure 2, one can see that the gap between the S_0 and S_1 states at $\phi = 90^\circ$ is larger than 1 eV. Thus, one should expect that other parameters will also be important in addition to the ϕ -twisting. Because we have neglected such additional elements, quantitative agreements should not be expected from our analysis. Of course, there are other potential causes for the lack of quantitative agreement: (1) the lack of polarizing electrostatic effect exerted on the IM subsystem by the MM system, (2) the approximate nature of starting structures of BFP variants, (3) some uncertainty in the protonation state of the

chromophore and its proximate residues, and (4) the limitations of the adopted conventional force field and our chromophore parametrizations in terms of nonbonded interactions. Nevertheless, it is encouraging to observe good correlations between the IM/MM simulation results and previous experimental data, as we have not attempted any optimizations with respect to experimental data and as we could generate the potential function of the chromophore in an automated manner.

The differences in the rotational dynamics will of course be affected by the protein–chromophore interaction. It has been discussed that the high mobility of the fluorophore is the cause of the low quantum yield in BFP.⁷⁴ With this argument, hindering the flexible twisting of the chromophore will be an important aspect for enhancing fluorescence.¹¹ Indeed, the mobility can be lowered by (1) tightly packing the protein cavity that surrounds the chromophore (steric blocking) or by (2) changing the electrostatic environment so that the chromophore rotation can feel resistance (Coulombic blocking). To unravel the roles of these two different types of nonbonded interactions toward the reduction of the chromophore mobility, we will analyze the role of dispersive van der Waals and Coulombic interactions toward the rotational dynamics in the following three sections.

Structural Features: Dispersive Interactions. The EBFP2.0 variant is different from EBFP1.2 in only four residues, as described in Table 2 and Figure 1e. However, its fluorescence property is noticeably enhanced, as shown in Table 2 and Figure 3. Thus, by investigating contributions of these four mutations toward hindering the chromophore rotation, we can gain insight on the role of the nonbonded interactions. First, we will check the detailed role of the four mutations on blocking the chromophore rotation by Lennard-Jones interaction. To do this, we have attempted to change the residues in a one-by-one manner. The resulting rotational dynamics are shown in Figure 4. We can see that all the mutations are doing their parts in the blocking, with an order of contributions of V224R > V150I > I128V > D155V. In addition, we can see that the two mostly contributing mutation sites are proximate to the chromophore (Figure 1e).

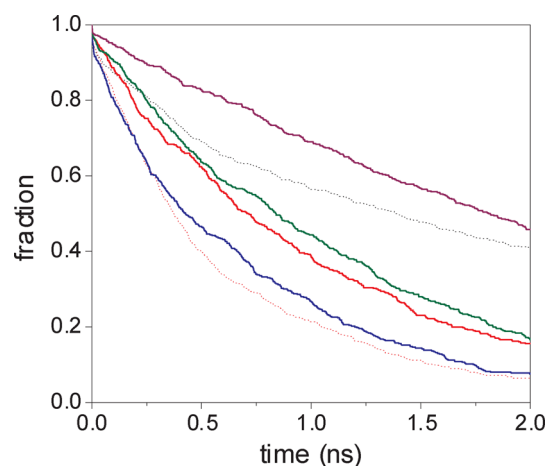


Figure 4. The fraction of nonrotated chromophores from 500 trajectories of I128V (red), V150I (green), D155V (blue), and V224R (purple). To facilitate direct comparisons, the behaviors of EBFP1.2 (dotted red) and EBFP2.0 (dotted black) as shown in Figure 3 are also presented.

To inspect how the mutations affect van der Waals interactions between the protein scaffold and the chromophore, we calculated the time progress of the Lennard-Jones interactions between the β -sheets and the imidazole ring. All the energies are of course calculated by averaging the obtained energies in 500 independent trajectories for the variants EBFP1.2, EBFP2.0, I128V, V150I, D155V, and V224R. We will adopt the same notations for the β -sheets as defined in the native BFP structure file (PDB ID: 2EMD).⁶⁸ The mutation sites I128V, D155V, V150I, and V224R are located in sheets β_3 , β_8 , $\beta_{8'}$, and β_{10} , respectively. Sheets β_7 – β_{10} are the closest ones to the chromophore, as indicated by the fact that the van der Waals energies originating from these sheets are much larger than the energies from other sheets (see Table S4, Supporting Information). Now the time progresses of the Lennard-Jones energies are plotted in Figure 5. Figure 5a displays the dispersion energies with all β sheets, and in all protein variants, the interaction energies are increasing with time. This means that the steric hindrance of the chromophore rotation is indeed present in all variants. In EBFP2.0 and all other mutants except

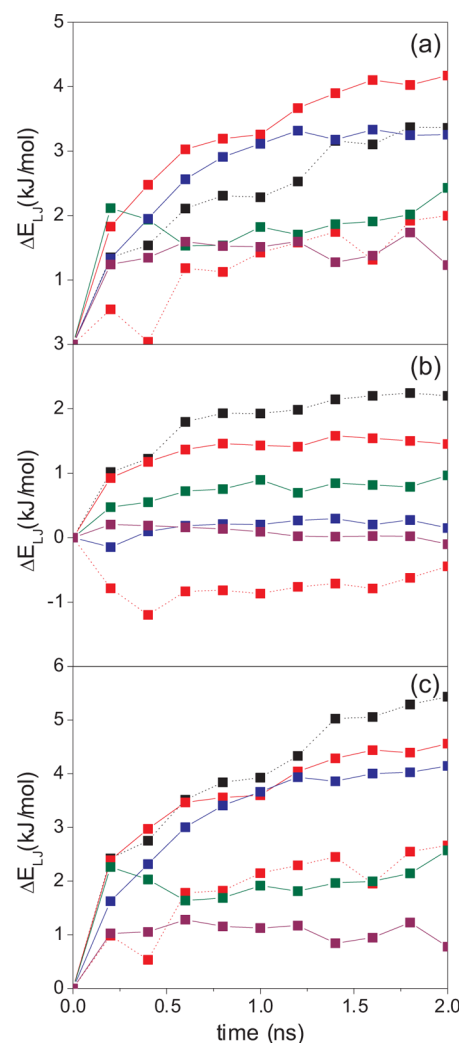


Figure 5. Time evolution of van der Waals interaction energies between the imidazole ring part of the chromophore and (a) all 10 β -sheets, (b) β_8 -sheet, and (c) β_7 – β_{10} sheets. The adopted proteins are I128V (solid red), V150I (green), D155V (blue), V224R (purple), EBFP1.2 (dotted red), and EBFP2.0 (dotted black).

V224R, this repelling effect is in general stronger than in EBFP1.2. At a first glance, it may be odd that the Arg residue with a larger side chain than Val has a reduced steric repulsion. We will defer the explanation of this exceptional behavior in V224R to the next section with the considerations of Coulombic interactions.

By decomposing the interaction energies between the chromophore and the β -barrel into a sheet-by-sheet manner, we can also investigate more details of the structural aspects. Out of many possibilities, the time progress of the dispersion interaction between the β_8 sheet and the imidazole ring is most intriguing and is shown in Figure 5b. Here, we can see that the interaction energy decreases in EBFP1.2, while it increases with V150I, I128V, and EBFP2.0. V224R or D155V mutation does not affect the β_8 -imidazole interaction to any significant extent. In the case of V150I, it is not surprising to see a noticeable level of steric rotation hindering with β_8 , because the residue 150 is accommodated in this sheet. Simply, a bulkier side chain will likely contribute more to the hindering. However, I128V is in β_3 and will unlikely directly affect the character of β_8 . We believe that V128 has an indirect effect by forcing β_8 closer to the chromophore. In EBFP2.0, these two aspects will cooperate. Namely, the V128 mutation will move β_8 closer to the chromophore, and I150 on β_8 will directly block the chromophore rotation. Additionally, although the residue-155 is on β_8 , the effect of D155V mutation is almost negligible. This is actually quite understandable because Val is not larger in size than Asp.

Finally, the time evolutions of the dispersive interaction energies exerted by β_7 – β_{10} sheets are shown in Figure 5c. As stated in the above, these sheets are the closest ones to the chromophore. Again, the rotational barrier generated by I128V mutation is quite higher than in EBFP1.2, even though the residue-128 is in β_3 . It is likely that this mutation is forcing these proximate sheets toward the chromophore. Somewhat surprisingly, D155V mutation on β_8 generates some energetic barrier with β_7 – β_{10} sheets even though the interaction with β_8 itself was not significantly altered, as stated above. Thus, D155V has an indirect effect possibly through electrostatic interaction modulation with other β -sheets. Again, the dispersive interaction in V224R mutant is found to be smaller than that in EBFP1.2. This means that the steric blocking contributes only negligibly in the V224R mutant protein. In fact, the major role of the V224R mutation is the modulation on the Coulombic interaction, as will be discussed in the following section.

Structural Features: Coulombic Interactions. With the atomic partial charges of the BFP chromophore (Table S2, Supporting Information), we can notice that the rotating imidazole ring and its bridge are overall positively charged in the excited state. More specifically, the partial charge of the group changes from $-0.115e$ in the ground state to $+0.615e$ in the excited state. Thus, it is natural to expect a repelling interaction between the chromophore and the R224 residue, which EBFP2.0 and azurite accommodate in the place of V224. To analyze how this interaction is affecting the rotational dynamics, we have calculated the electrostatic energy between the rotating imidazole moiety and the side chain of R224/V224. Figure 6 shows the average time evolutions of these Coulombic interactions taken from the 500 independent trajectories for the four protein variants. As expected, EBFP2.0 and azurite with R224 exhibit quite a strong repelling aspect, while BFP and EBFP1.2 do not show any significant changes in the

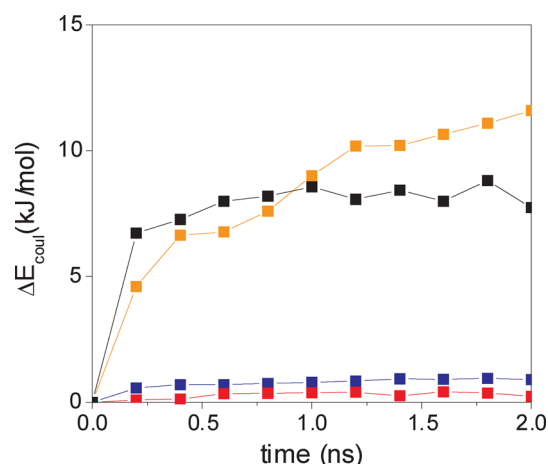


Figure 6. Time evolution of electrostatic interaction energies between V/R224 and the rotating imidazole ring. Adopted proteins are BFP (blue), azurite (orange), EBFP1.2 (red), and EBFP2.0 (black).

electrostatic interaction. This clearly shows that the electrostatic interaction between the Arg residue and the chromophore plays a crucial role in deterring the imidazole ring rotation and in improving the fluorescence characteristics.

Up to this point, we have analyzed the structural contributions from the mutations to the fluorescence enhancement. D155V and I128V mutations tune the protein environment so that dispersive interactions between the chromophore and β -sheets can hinder the twisting of the chromophore. V150I directly obstructs the twisting by van der Waals interactions, and V224R mainly contributes through electrostatic interactions. These aspects appear to be nicely combined in EBFP2.0, and highly optimized fluorescence enhancement is obtained through these cooperative effects.

Time Resolved Analysis of the Roles of Steric and Coulombic Interactions: Rotation-Rate Analysis. As stated in the above, we have shown that both steric and Coulombic interactions contribute to slowing down the twisting of the chromophore part. Will these two interactions contribute in a concurrent or separated manner in time? To inspect this aspect, we need to isolate one effect from the other. For this purpose, we have generated two additional computational mutants by resetting the partial charges of the side chain atoms to zero at residues 128, 150, 155, and 224 on both EBFP1.2 and EBFP2.0. These “uncharged” variants will be denoted as EBFP1.2-UC and EBFP2.0-UC, respectively. The fractions of nonrotated chromophores for these mutants are plotted in Figure 7a. Comparing the uncharged variants against their corresponding charged variants, we can again see that the hindering effect generated by the electrostatic interactions is quite important. To facilitate more detailed comparisons, the rate constant (k) for chromophore rotations⁷⁵ for each variant was calculated as a function of time. For this purpose, the time progress of the nonrotated chromophore fraction (N_{nr}/N_{tot}) in each variant was fit with three exponential functions.⁷⁶ The rotation rate, $v = -dN_{nr}/dt$, was then calculated by taking the time derivative of this fitted function. Of course, the rate constant at any time point can be obtained by normalizing the rate by the number of protein molecules with nonrotated chromophores, namely, $k = v/N_{nr}$. The rate constant computed in this manner reflects the twisting propensity of the chromophore at any given time, and is presented in Figure 7b.

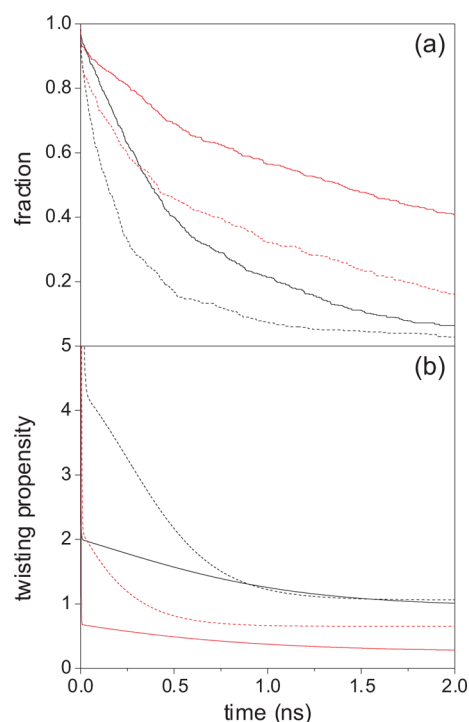


Figure 7. (a) The fraction of the nonrotated chromophores from 500 trajectories of EBFP1.2 (solid black), EBFP2.0 (solid red), EBFP1.2-UC (dashed black), and EBFP2.0-UC (dashed red). (b) Twisting propensities of the chromophore in the four proteins as defined by the rotation rate constants.

From the obtained twisting propensities, the contributions of the two different types of nonbonded interactions on the chromophore internal rotation can be inferred in a separate manner. We will mainly focus on reasoning the performance improvement in EBFP2.0. First, by comparing k values of EBFP1.2-UC and EBFP2.0-UC, the contribution of the steric interaction in EBFP2.0 can be estimated separately from the Coulombic interaction at least in a qualitative way. With the comparison, we can see that the reduction in the twisting propensity in EBFP2.0-UC is larger in earlier time. Thus, the steric effect appears to participate more importantly in the early stage after photoexcitation. Next, in the EBFP1.2 case, we can observe that the reduction in twisting propensity over EBFP1.2-UC disappears after ~ 1 ns. On the contrary, in the EBFP2.0 case, the same reduction over EBFP2.0-UC lasts much longer. This implies that the improvement in EBFP2.0 by the Coulombic interaction has a lasting effect in time. It is interesting to note that the propensity reduction in EBFP2.0 over EBFP2.0-UC in the early stage is much smaller than the reduction in EBFP1.2 over EBFP1.2-UC. This additionally supports the view that the Coulomb interaction modification in EBFP2.0 participates in the late stage after the photoexcitation. The time scale difference is likely due to the longer ranged nature of Coulombic interaction compared against the dispersion interaction.

4. CONCLUDING REMARKS

We have proposed an interpolated mechanics–molecular mechanics (IM/MM) scheme for potential energy surface constructions and applied it to investigating the excited state dynamics of the blue fluorescent protein. For constructing the surface, we have first fitted the atomic partial charges and the

Lennard-Jones potential parameters with a relatively small number of quantum chemically calculated data. For the purpose of demonstrating the reliability of the present IM/MM scheme, we have adopted a small and qualitatively correct (4,4) active space scheme for generating a data set with calculations of the BFP chromophore. The interpolation data set, with the potentials and their first and second derivatives, could be semiautomatically generated except at some geometries, where the proper CASSCF solutions were not found at first trials. We have also added corrections for the dynamic electron correlation effect by resorting to the dual-level interpolation scheme.³⁷ By calculating the fraction of nonrotated chromophores in time, we have shown that much of the fluorescence properties of BFP variants could be reproduced, with at least qualitative agreements with the data obtained from experimentally observed quantum yield and fluorescence lifetime. We also investigated how the mutation induced structural changes affect the chromophore twisting dynamics by considering the Lennard-Jones interactions between protein β -sheets and the chromophore. From this, we concluded that not only the steric interactions from proximate residues but also the somewhat distant protein environment are cooperatively hindering the internal rotation of the chromophore. We also inspected the roles of the Coulombic and dispersion interactions to enhancing fluorescence in EBFP2.0. The two effects were participating in hindering the chromophore rotation, but their timings were different.

Using the IM/MM based molecular dynamics simulations, we have conducted excited state trajectory calculations over 10 μ s of aggregate simulation time. This lengthy simulation will not be practically possible with the more conventional QM/MM approach. Even though we have observed good qualitative agreements with previous experimental findings, we did see discrepancies in the quantitative sense. The major cause of the quantitative disagreement will likely stem from inaccuracies of the adopted potential energy surface. At least in principle, this shortcoming can be fixed by adopting a more reliable quantum chemical approach with a better electron correlation scheme. Simplifying nonadiabatic and nonradiative decays with only chromophore twisting on a single surface is also an important limitation of our present approach. Because applying the interpolation scheme for full nonadiabatic dynamics is also possible in principle,^{50,51} this issue is also a technical one. Other possible causes of the errors are the limitations in treating electrostatic interactions between the IM and MM areas, the approximate nature of the protein structures of the BFP variants, the rather ambiguous protonation state of the chromophore and its nearby residues, and the lack of polarizability in the force field description of the MM part. When these issues are more appropriately addressed, we believe that better quantitative agreements with the experimental results will be attained. In any case, we feel that it is encouraging to observe good qualitative agreements even though we have adopted a quite small size of active space and did not attempt to parametrize any variables with respect to experimental data. Thus, we hope that our approach will be useful for future studies on the dynamics of various fluorescent proteins and other related photoproteins. Inclusions of nonadiabatic aspects will be particularly important for such studies toward more complete descriptions of the dynamics.

■ ASSOCIATED CONTENT

■ Supporting Information

Complete citations of refs 7 and 62, the details of our approach of obtaining well-behaved solution in CASSCF calculation, characteristics and shapes of the active orbitals included in SA2-CAS(4,4) calculations, fitted RESP charges and Lennard-Jones parameters for the BFP chromophore, fitted multiexponential parameters of nonrotated chromophore fraction, and Lennard-Jones interaction energies between individual β -sheets and the chromophore right at the photoexcitation. This material is available free of charge via the Internet at <http://pubs.acs.org>.

■ AUTHOR INFORMATION

Corresponding Author

*E-mail: yrmhee@postech.ac.kr.

Notes

The authors declare no competing financial interest.

■ ACKNOWLEDGMENTS

This work was supported by Basic Science Research Program (Grant No. 2011-0023393) and by WCU Program (Grant No. R32-2008-000-10180-0) through the National Research Foundation of Korea (NRF) funded by the Ministry of Education, Science, and Technology. The supercomputer time from Korea Institute of Science and Technology Information (KISTI) under Grant No. KSC-2012-C3-04 is also gratefully acknowledged.

■ REFERENCES

- (1) Allen, M. P.; Tildesley, D. J. *Computer Simulation of Liquids*; Oxford University Press: Oxford, U.K., 1987.
- (2) Leach, A. R. *Molecular Modelling: Principles and Applications*; Pearson Education Limited: Harlow, U.K., 2001.
- (3) Frenkel, D.; Smit, B. *Understanding Molecular Simulations*; Academic Press: London, 2002.
- (4) Karplus, M.; McCammon, A. J. *Nat. Struct. Biol.* **2002**, *9*, 646–652.
- (5) Hornak, V.; Abel, R.; Okur, A.; Strockbine, B.; Roitberg, A.; Simmerling, C. *Proteins* **2006**, *65*, 712–725.
- (6) Jorgensen, W. L.; Maxwell, D. S.; Tirado-Rives, J. *J. Am. Chem. Soc.* **1996**, *118*, 11225–11236.
- (7) MacKerell, A. D., Jr.; Bashford, D.; Bellott, M.; Dunbrack, R. L., Jr.; Evanseck, J. D.; Field, M. J.; Fischer, S.; Gao, J.; Guo, H.; Ha, S. J. *Phys. Chem. B* **1998**, *102*, 3586–3616.
- (8) Remington, S. J. *Methods Enzymol.* **2000**, *305*, 196–211.
- (9) Lopez, X.; Margues, M. A. L.; Castro, A.; Rubio, A. *J. Am. Chem. Soc.* **2005**, *127*, 12329–12337.
- (10) Heim, R.; Prasher, D. C.; Tsien, R. Y. *Proc. Natl. Acad. Sci. U.S.A.* **1994**, *91*, 12501–12504.
- (11) Mena, M. A.; Treynor, T. P.; Mayo, S. L.; Daugherty, P. S. *Nat. Biotechnol.* **2006**, *24*, 1569–1571.
- (12) Ai, H.-W.; Shaner, N. C.; Cheng, Z.; Tsien, R. Y.; Campbell, R. E. *Biochemistry* **2007**, *46*, 5904–5910.
- (13) Day, R. N.; Davidson, M. W. *Chem. Soc. Rev.* **2009**, *38*, 2887–2921.
- (14) Ai, H.-W.; Henderson, J. N.; Remington, S. J.; Campbell, R. E. *Biochem. J.* **2006**, *400*, 531–540.
- (15) Remington, S. J. *Curr. Opin. Struct. Biol.* **2006**, *16*, 714–721.
- (16) Pakhomov, A. A.; Martynov, V. I. *Chem. Biol.* **2008**, *15*, 755–764.
- (17) Hasegawa, J.-Y.; Ise, T.; Fujimoto, K. J.; Kikuchi, A.; Fukumura, E.; Miyawaki, A.; Shiro, Y. *J. Phys. Chem. B* **2010**, *114*, 2971–2979.
- (18) Tsien, R. Y. *Annu. Rev. Biochem.* **1998**, *67*, 509–544.
- (19) Verkhusha, V. V.; Lukyanov, K. A. *Nat. Biotechnol.* **2004**, *22*, 289–296.
- (20) Meech, S. R. *Chem. Soc. Rev.* **2009**, *38*, 2922–2934.
- (21) Martin, M. E.; Negri, F.; Olivucci, M. J. *Am. Chem. Soc.* **2004**, *126*, 5452–5464.
- (22) Megly, C. M.; Dickson, L. A.; Maddalo, S. L.; Chandler, G. J.; Zimmer, M. J. *Phys. Chem. B* **2009**, *113*, 302–308.
- (23) van Thor, J. J. *Chem. Soc. Rev.* **2009**, *38*, 2935–2950.
- (24) Jonasson, G.; Teuler, J.-M.; Vallverdu, G.; Mérola, F.; Ridard, J.; Lévy, B.; Demachy, I. *J. Chem. Theory Comput.* **2011**, *7*, 1990–1997.
- (25) Olsen, S.; Lamothe, K.; Martínez, T. J. *J. Am. Chem. Soc.* **2010**, *132*, 1192–1193.
- (26) Virshup, A. M.; Punwong, C.; Pogorelov, T. V.; Lindquist, B. A.; Ko, C.; Martínez, T. J. *J. Phys. Chem. B* **2009**, *113*, 3280–3291.
- (27) Hasegawa, J.-Y.; Fujimoto, K.; Swerts, B.; Miyahara, T.; Nakatsuji, H. *J. Comput. Chem.* **2007**, *28*, 2443–2452.
- (28) Olsen, S.; Smith, S. C. *J. Am. Chem. Soc.* **2008**, *130*, 8677–8689.
- (29) Li, X.; Chung, L. W.; Mizuno, H.; Miyawaki, A.; Morokuma, K. *J. Phys. Chem. B* **2010**, *114*, 16666–16675.
- (30) Li, X.; Chung, L. W.; Mizuno, H.; Miyawaki, A.; Morokuma, K. *J. Phys. Chem. Lett.* **2010**, *1*, 3328–3333.
- (31) Hasegawa, J.-Y.; Fujimoto, K. J.; Nakatsuji, H. *ChemPhysChem* **2011**, *12*, 3106–3115.
- (32) Polyakov, I.; Epifanovsky, E.; Grigorenko, B. L.; Krylov, A. I.; Nemukhin, A. V. *J. Chem. Theory Comput.* **2009**, *5*, 1907–1914.
- (33) Bravaya, K. B.; Khrenova, M. G.; Grigorenko, B. L.; Nemukhin, A. V.; Krylov, A. I. *J. Phys. Chem. B* **2011**, *115*, 8296–8303.
- (34) Ischtwan, J.; Collins, M. A. *J. Chem. Phys.* **1994**, *100*, 8080–8088.
- (35) Rhee, Y. M.; Lee, T. G.; Park, S. C.; Kim, M. S. *J. Chem. Phys.* **1997**, *106*, 1003–1012.
- (36) Rhee, Y. M. *J. Chem. Phys.* **2000**, *113*, 6021–6024.
- (37) Nguyen, K. A.; Rossi, I.; Truhlar, D. G. *J. Chem. Phys.* **1995**, *103*, 5522–5530.
- (38) Ho, T.-S.; Hollebeek, T.; Rabitz, H.; Harding, L. B.; Schatz, G. C. *J. Chem. Phys.* **1996**, *105*, 10472–10486.
- (39) Thompson, K. C.; Jordan, M. J. T.; Collins, M. A. *J. Chem. Phys.* **1998**, *108*, 564–578.
- (40) Thompson, K. C.; Jordan, M. J. T.; Collins, M. A. *J. Chem. Phys.* **1998**, *108*, 8302–8316.
- (41) Bettens, R. P. A.; Collins, M. A. *J. Chem. Phys.* **1999**, *111*, 816–826.
- (42) Bettens, R. P. A.; Hansen, T. A.; Collins, M. A. *J. Chem. Phys.* **1999**, *111*, 6322–6332.
- (43) Fuller, R. O.; Bettens, R. P. A.; Collins, M. A. *J. Chem. Phys.* **2001**, *114*, 10711–10716.
- (44) Moyano, G. E.; Collins, M. A. *J. Chem. Phys.* **2003**, *119*, 5510–5517.
- (45) Higashi, M.; Truhlar, D. G. *J. Chem. Theory Comput.* **2009**, *5*, 2925–2929.
- (46) Higashi, M.; Truhlar, D. G. *J. Chem. Theory Comput.* **2008**, *4*, 1032–1039.
- (47) Higashi, M.; Truhlar, D. G. *J. Chem. Theory Comput.* **2008**, *4*, 790–803.
- (48) Lin, H.; Zhao, Y.; Tishchenko, O.; Truhlar, D. G. *J. Chem. Theory Comput.* **2006**, *2*, 1237–1254.
- (49) Park, J. W.; Kim, H. W.; Song, C.-I.; Rhee, Y. M. *J. Chem. Phys.* **2011**, *135*, 014107.
- (50) Godsi, O.; Evenhuis, C. R.; Collins, M. A. *J. Chem. Phys.* **2006**, *125*, 104105.
- (51) Evenhuis, C.; Martínez, T. J. *J. Chem. Phys.* **2011**, *135*, 224110.
- (52) Finley, J.; Malmqvist, P.-Å.; Roos, B. O.; Serrano-Andrés, L. *Chem. Phys. Lett.* **1998**, *288*, 299–306.
- (53) Singh, U. C.; Kollman, P. A. *J. Comput. Chem.* **1986**, *7*, 718–730.
- (54) Field, M. J.; Bash, P. A.; Karplus, M. *J. Comput. Chem.* **1989**, *11*, 700–733.
- (55) Stårling, J.; Bernhardsson, A.; Lindh, R. *Mol. Phys.* **2001**, *99*, 103–114.
- (56) Widmark, P.-O.; Malmqvist, P.-Å.; Roos, B. O. *Theor. Chim. Acta* **1990**, *77*, 291–306.

- (57) Roos, B. O.; Lindh, R.; Malmqvist, P.-Å.; Veryazov, V.; Widmark, P.-O. *J. Phys. Chem. A* **2004**, *108*, 2851–2858.
- (58) Bayly, C. I.; Cieplak, P.; Cornell, W.; Kollman, P. A. *J. Phys. Chem.* **1993**, *97*, 10269–10280.
- (59) Song, C.-I.; Rhee, Y. M. *Int. J. Quantum Chem.* **2011**, *111*, 4091–4105.
- (60) Song, C.-I.; Rhee, Y. M. *J. Am. Chem. Soc.* **2011**, *133*, 12040–12049.
- (61) In building the data set, the Pople basis set of 6-31+G* was adopted instead of the ANO basis set mainly due to its lower computational cost. The energy difference induced by the basis set difference was rather small, and should not be that important considering the more approximate nature of the adopted active space scheme.
- (62) Werner, H.-J.; Knowles, P. J.; Lindh, R.; Manby, F. R.; Schütz, M.; Celani, P.; Korona, T.; Mitrushenkov, A.; Adler, T. B.; Amos, R. D.; et al. *MOLPRO: a package of ab initio programs*, version 2009.1; University College Cardiff: Cardiff, U. K., 2009.
- (63) Angeli, C.; Calzado, C. J.; Cimiraglia, R.; Evangelisti, S.; Mayna, D. *Mol. Phys.* **2003**, *101*, 1937–1944.
- (64) Slaviček, P.; Martínez, T. J. *J. Chem. Phys.* **2010**, *132*, 234102.
- (65) Hess, B.; Kutzner, C.; van der Spoel, D.; Lindahl, E. *J. Chem. Theory Comput.* **2008**, *4*, 435–447.
- (66) DePaul, A. J.; Thompson, E. J.; Patel, S. S.; Haldeman, K.; Sorin, E. J. *Nucleic Acids Res.* **2010**, *38*, 4856–4867.
- (67) Hess, B.; Bekker, H.; Berendsen, H. J. C.; Fraaije, J. G. E. M. *J. Comput. Chem.* **1997**, *18*, 1463–1472.
- (68) Palm, G. J.; Zdanov, A.; Gaitanaris, G. A.; Stauber, R.; Pavlakis, G. N.; Wlodawer, A. *Nat. Struct. Biol.* **1997**, *4*, 361–365.
- (69) Dolinsky, T. J.; Nielsen, J. E.; McCammon, A. J.; Baker, N. A. *Nucleic Acids Res.* **2004**, *32*, W665–W667.
- (70) Fletcher, R. *Practical Methods of Optimization*; Wiley: New York, 1987.
- (71) Berendsen, H. J. C.; Postma, J. P. M.; van Gunsteren, W. F.; DiNola, A.; Haak, J. R. *J. Chem. Phys.* **1984**, *81*, 3684–3690.
- (72) Nosé, S. *J. Chem. Phys.* **1984**, *81*, 511–519.
- (73) Parrinello, M.; Rahman, A. *J. Appl. Phys.* **1981**, *52*, 7182–7190.
- (74) Muring, K.; Deich, J.; Rossell, F. I.; McAnaney, T. B.; Moerner, W. E.; Boxer, S. G. *J. Phys. Chem. B* **2005**, *109*, 12976–12981.
- (75) The “rotation rate” described here refers to the rate of the population change of the rotated chromophore, and is different from the rotation speed.
- (76) The purpose of this fit was to eliminate the numerical noise from the limited number of simulations. The fitting coefficients and the reliabilities of the fits are shown in Table S3 and Figure S2 in the Supporting Information.
- (77) Subach, O. M.; Gundorov, I. S.; Yoshimura, M.; Subach, F. V.; Zhang, J.; Grünwald, D.; Souslova, E. A.; Chudakov, D. M.; Verkhusha, V. V. *Chem. Biol.* **2008**, *15*, 1116–1124.
- (78) Drobizhev, M.; Makarov, N. S.; Tillo, S. E.; Hughes, T. E.; Rebane, A. *Nat. Methods* **2011**, *8*, 393–399.
- (79) Tillo, S. E.; Hughes, T. E.; Makarov, N. S.; Rebane, A.; Drobizhev, M. *BMC Biotechnol.* **2010**, *10*, 6.